IEEE Access
Multidisciplinary | Rapid Review | Open Access Journal

Received May 21, 2019, accepted June 13, 2019, date of publication July 1, 2019, date of current version July 16, 2019.

Digital Object Identifier 10.1109/ACCESS.2019.2926102

Placement of Sub-Resolution Assist Features Based on a Genetic Algorithm

WEI-MING KAN[1], YU-RU HUANG[1], CHAO-YI HUANG[2], CHUN-SHENG WU[2], KAO-TUN CHEN[2], YU-SHIN LIN[3], AND HUNG-FEI KUO[1]

[1]Graduate Institute of Automation and Control, National Taiwan University of Science and Technology, Taipei 106, Taiwan
[2]Winbond Electronics Corporation, Taichung 428, Taiwan
[3]Shuz Tung Machinery Industrial Company Ltd., Taichung 421, Taiwan

Corresponding author: Hung-Fei Kuo (hfkuo@mail.ntust.edu.tw)

This work was supported in part by the Ministry of Science and Technology of Taiwan under Project MOST 107-2218-E-011-025, and in part by the Ministry of Economic Affairs of Taiwan under Project 104-EC-17-A-05-I4-0006.

ABSTRACT Resolution enhancement techniques compatible with an ArF (193 nm) immersion optical lithography system may constitute an effective means of minimizing the size of technology nodes of the dynamic random access memory. This paper investigated one such technique, namely mask optimization (MO), and applied sub-resolution assist features (SRAFs) in the MO to improve the aerial image quality of a target pattern that had undergone optical proximity correction (OPC). This paper first developed an optical model based on the Hopkins model to create an interference map, which was then used to create a cut-level map. The cut-level map was instrumental in predicting potential SRAF sites and randomly generating SRAFs that would serve as the initial population for a genetic algorithm (GA). Chromosomes were defined as a section map and encoded genes were used to define SRAF and target pattern. Using a GA to identify SRAF geometric measurements and placement was revealed to increase the process window and improve the image performance of the target pattern. This paper used 1D and 2D line/space (L/S) images as the baseline to test the convergence of the proposed method. 2D images were also used to test improvements in aerial image performance. The results indicated that the 1D L/S pattern converged at the 100th iteration. Furthermore, the depths of the focus of the 2D L/S array and 2D contact hole patterns were successfully increased by 113 and 21 nm, respectively. The proposed SRAF method, which integrated the GA and interference map, was able to ensure the diversity of potential SRAF solutions. Moreover, it was able to restrict the SRAF solutions to rectangular structures through the application of mask rules, thereby reducing the cost and improving the feasibility of photomasks.

INDEX TERMS Sub-resolution assist feature (SRAF), interference map, genetic algorithm (GA), mask optimization, depth of focus (DOF).

I. INTRODUCTION

Dynamic random access memory (DRAM) is extensively used in components for smart televisions, self-driving cars, internet of things applications, and high-end servers, rendering the continual minimization of DRAM technology nodes a critical task [1], [2]. Optical lithography, as a key step in the manufacturing of DRAM components, primarily relies on the ArF (193 nm) immersion optical lithography system, a system with a consistently high yield and high resolution in mass production [3]–[5]. However, when attempting to progressively shrink the critical dimension (CD) of a device by applying Moore's Law, resolution enhancement technology (RET) must be implemented to improve the quality of images projected on the photoresist.

Common RET techniques include mask optimization (MO), source optimization, double patterning, and directed self-assembly [6]–[9]. MO is used to solve the optical proximity error, thereby preventing aerial image distortion induced by a severe diffraction effect. To this end, the target pattern is corrected to meet the desired lithography process results in a procedure commonly referred to as optical proximity correction (OPC) [10], [11]. However, OPC alone cannot guarantee an effective increase in the process window, and can even lead to reduced processing efficiency. Therefore, sub-resolution assist features (SRAFs) must be introduced to

The associate editor coordinating the review of this manuscript and approving it for publication was Rahul A. Trivedi.

further increase the process window [12], [13]. For example, the addition of attenuated assist features can improve the depth of focus (DOF) of the isolated line pattern, and the placement of SRAFs in the sidelobes can intensify the contrast of the dense pattern, thereby increasing the process window.

Many methods have been proposed for placing SRAFs in the photomask: Melvin *et al.* and others have used the difference between the aerial image intensity of the focal plane and that outside of the focal plane to generate a focus sensitivity map for determining sites for SRAF placement [14]–[16]. The results revealed an increase in DOF of the isolated contact holes by more than 400 nm. Kawashima *et al.* and Hakko*et al.*used the two-dimensional transmission cross coefficient (2D-TCC) technique as the basis for an algorithm [17], [18] and discovered that the simplified optical model could quickly determine potential SRAF sites and apply these in OPC. However, the technique was unable to further enhance the quality of aerial images, and the gradient descent algorithm used further complicated the computation by requiring the calculation of the gradient between an optimized target pattern and the corrected photomask [19], [20]. Moreover, the optimized target pattern in this design was primarily measured by the main focus and main exposure dose, meaning that it could not guarantee an increase in the process window. To address these shortcomings, Xu *et al.* proposed applying a genetic algorithm (GA) to both positive and negative SRAF placement rules [21], [22]. This approach, which applies a GA for searching SRAF sites, utilizes a fitness function as an indicator to reduce SRAF printability, thereby producing superior results to those of model-based SRAF placement. However, the drawback of relying on rule-based SRAF placement is that it lacks diversity, making it prone to converging to local optimal solutions.

This study integrated the intensity map with the mask rules on the focal plane to determine SRAF sites and employed a GA to identify the optimal image quality and maximize the process window. This approach differed from the conventional method and prevented the development of overly complicated SRAF structures, thus reducing the manufacturing cost of the photomask. In this paper, Section II describes the proposed optical model, Section III explains the GA-based SRAF design, Section IV examines the aerial image quality of the 2D mask pattern using the SRAF algorithm, and Section V provides the research conclusions.

II. PROJECTION LITHOGRAPH MODEL

The MO process consists of two parts: the first part involves the OPC for the pre-OPC target pattern, and the second part involves the addition of SRAFs in the post-OPC target formed upon completion of the OPC for the target pattern [23], [24]. The first part of this study used KLA-Tencor PROLITH for the OPC results of the pre-OPC target. The post-OPC target results were then combined with SRAFs developed by the research team to complete the MO process. The performance of the aerial images for the target pattern was assessed using

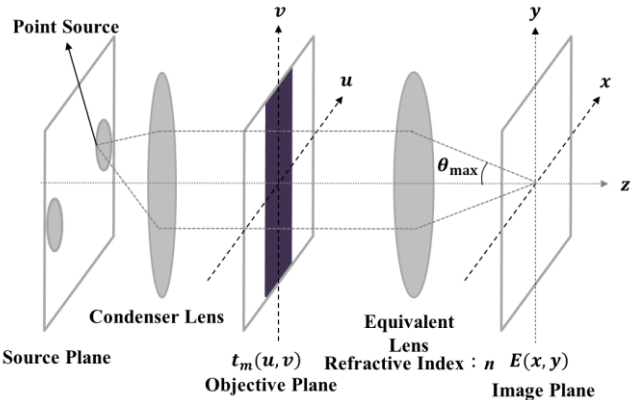

FIGURE 1. Conceptual optical lithography system.

lithography metrics. This section discusses the development of an optical model for the optical lithography system.

Fig. 1 illustrates the projection lithography system model used in this study [25]. The spherical wave created by an arbitrary point source on the source plane passes through the condenser lens and is converted into a plane wave that is incident onto the photomask situated on the objective plane. The electric field before the incidence of the photomask is denoted as $E_i(x, y)$, (u, v) denotes the coordinates of the objective plane, $t_m(u, v) = te^{i\theta}$ is the transmittance function of the light passing through the photomask, t denotes the transmittance, and θ denotes the phase. $t = 1$ indicates that the photomask has full light transparency and $t = 0$ means that the mask has full opacity. The diffracted beams by the patterns on the photomask are collected by the equivalent lens, forming the interfering electric field $E(x, y)$ on the image plane. Assuming that the refractive index of the equivalent lens is n and the numerical aperture $(NA) = n\theta_{\max}$ for the entire optical system, the spatial coordinate (u, v) corresponds to the spatial frequency coordinate (f_u, f_v), which has (g_u, g_v) as its Hermitian coordinate.

The optical model based on the system illustrated in Fig. 1 can be converted into (1) using the Hopkins model [26]–[28].

$$I(x, y) = \sum_{f_u, f_v, g_u, g_v} TCC(f_u, f_v, g_u, g_v) \times T_m(f_u, f_v)\, T_m^*(g_u, g_v)\, e^{\{-i2\pi[(f_u - g_u)x + (f_v - g_v)y]\}} \quad (1)$$

where $I(x, y)$ is the aerial image intensity at (x, y) on the image plane and TCC can be expressed as (2), which contains the expressions of both the pupil function P and source shape S in the frequency domain. Additionally, (g_u, g_v) represents the Hermitian coordinate of the pupil function P, and (δ_1, δ_2) represents the spatial frequency domain coordinate of the source shape S.

$$TCC(f_u, f_v, g_u, g_v) = \sum_{\delta_1, \delta_2} P(f_u + \delta_1, f_v + \delta_2) \times P^*(g_u + \delta_1, g_v + \delta_2)\, S(\delta_1, \delta_2) \quad (2)$$

For the rapid calculation of aerial image intensity, this study adopted the 2D-TCC technique [29], [30], which converts the TCC function in (2) into a $W_{s,t}(g_u, g_v)$ function for the approximation of aerial image intensity. Specifically, it fixes the two spatial frequency variables in the TCC function of (2), f_u and g_v, in (s, t) as (3). After the variables have been simplified, $W_{s,t}(g_u, g_v)$, which is no longer a four-dimensional array, is substituted into (1) to yield its product with $T_{\mathrm{m}}^*(g_u, g_v)$, the Hermitian transformation of the photomask's frequency domain, and thus undergo inverse Fourier transformation. $I(x, y)$ can be expressed as (4) and further reduced to the sum of discrete components $Y_{s,t}(x, y)$ using the 2D-TCC function. When only a partial coherence source is considered (i.e., when for the partial coherence factor, σ), the pupil function can fully include effective light sources and $W_{0,0}(g_u, g_v)$ can be expressed as (5) under the condition $(s, t) = (0, 0)$. By substituting (5) into (4), the aerial image intensity can be approximated as $Y_{0,0}$ (x, y) in (6). This $Y_{0,0}$ (x, y) is referred to as the interference map. In (6), $\Gamma_0(x, y)$ represents the light intensity distribution of the light transmitted from a point source on the source plane to the objective plane. It is also the Fourier transformation of an effective light source S [31]. The Fourier transformation of the pupil function is the impulse response in the imaging system. An impulse response represents the transmission from a point on the objective plane to the source plane and is also regarded as the superposition of plane waves. Therefore, (6) clearly indicates that $Y_{0,0}$ is the approximation of the convolution of the response to the source S at the image plane and the photomask pattern.

The interference map is regarded as the result of photomask-induced diffraction beams interfere with each other on the image plane. Therefore, because the combined effect of both the constructive interference and destructive interference can be observed in the aerial image intensity calculated using (6), the interference map can be considered to indicate possible sites for SRAF placement [32], [33]. The interference map model based on (6) can be explained using the one-dimensional line/space (1D L/S) pattern. Fig. 2(a) displays a dipolar test source, and Fig. 2(b) reveals the test L/S pattern, in which the line is 45 nm in width and the pitch is 300 nm. Fig. 2(c) shows the interference map calculated using (6), and Fig. 2(d) presents the cut-level map generated by removing the sidelobe areas in the interference map after a threshold value has been set. Excluding the target pattern in the center, the remaining four yellow rectangles are possible sites for SRAF placement. By placing SRAFs on these sites, a composite photomask pattern that contains both the target pattern and the SRAFs can be formed. The aerial image produced by the SRAFs can significantly interfere with the aerial image intensity of the target pattern on the image plane, potentially improving the image resolution. The constructive interference areas in the approximated aerial image can be used to estimate the SRAF sites.

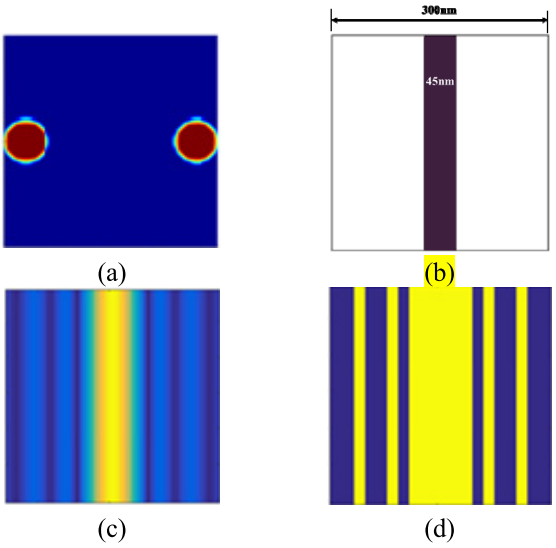

FIGURE 2. Converting the interference map to the cut-level map to predict potential sites for SRAF placement: (a) dipolar source; (b) target pattern; (c) interference map; (d) cut-level map.

$$W_{s,t}(g_u, g_v) = TCC(s, t, g_u, g_v) \tag{3}$$

$$I(x, y) = \sum_{s,t} T_m(s, t) e^{[-i2\pi(sx+ty)]} \mathcal{F}^{-1} \times [W_{s,t}(g_u, g_v) T_m^*(g_u, g_v)] \tag{4}$$

$$W_{0,0}(g_u, g_v) = S(g_u, g_v) \otimes P^*(g_u, g_v) \tag{5}$$

$$Y_{0,0}(x, y) = T_m(0, 0) \{\Gamma_0(x, y) \mathcal{F}[P(g_u, g_v)]\}^* \otimes t_m^*(x, y) \tag{6}$$

III. GA-BASED SRAF DESIGN

A GA was created to simulate the evolutional behaviors of organisms [34]–[36]. To adapt to environmental changes, organisms continually evolve through behaviors such as selection, crossover, and mutation. Because each individual organism carries chromosomes that bear its own unique genes, evolutional behaviors facilitate the exchange and variation of genes, resulting in the survival of the fittest genes. Applying this concept, the GA enables a large-scale search that produces multiple suitable solutions, from which the most suitable one is selected as the best solution [37]–[41]. This study used the GA to determine the optimal sites and geometric measurements of SRAFs for a photomask [42]–[45].

Fig. 3 conveys the process of applying the GA for optimal SRAF placement, which consists of generating the initial population, optimizing the SRAF, and screening for the optimal solution using mask rule checking (MRC). Two methods have been proposed for generating the initial population: the first is described in Section II and involves applying the 2D-TCC technique to calculate the interference map, which

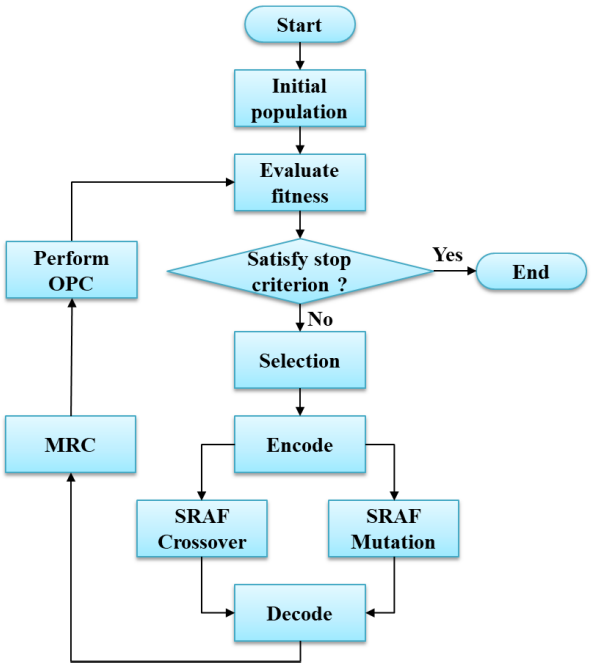

FIGURE 3. GA-based SRAF optimization flow design.

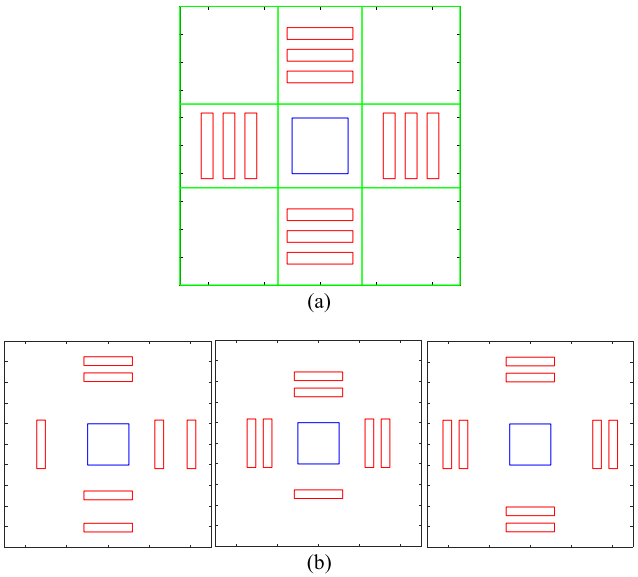

FIGURE 4. Random generation of SRAF candidates to be placed on the photomask with sites and geometric measurements that conform to the mask rules: (a) generating sections in the section map within the ROI; (b) randomly generating SRAF candidates and their layout patterns.

then serves as the basis for a cut-level map that indicates the sites and geometric measurements of potential SRAFs. The other method is the random generation of potential SRAFs, as demonstrated in Fig. 4: the blue rectangle represents the target pattern and the red rectangles represent the SRAFs. After the borders of the pre-OPC target and the region of interest (ROI) are defined, the area inside the ROI and adjacent to the pre-OPC target is separated into four subareas, as indicated by the areas within the green lines in Fig. 4(a), and defined as sections in the section map. In the section map, the sections adjacent to the pre-OPC target are located above, below, and to the left and right of the pre-OPC target. Each of these sections can further randomly generate red rectangles, which are potential sites for SRAF placement; the SRAF sites and geometric measurements must all conform to the mask rules. Furthermore, the arrangement of the SRAF rectangles must obey the following principles: the SRAF rectangles in the sections to the left and right of the pre-OPC target must be parallel to the *y*-axis, whereas those in the sections above and below the pre-OPC target must be parallel to the *x*-axis. After the SRAFs have been randomly generated, the SRAFs obtained through the first and second methods are separately coupled with the target pattern (post-OPC target) corrected by the OPC model to form different photomask patterns. These photomask patterns can then be used to determine the corresponding aerial images.

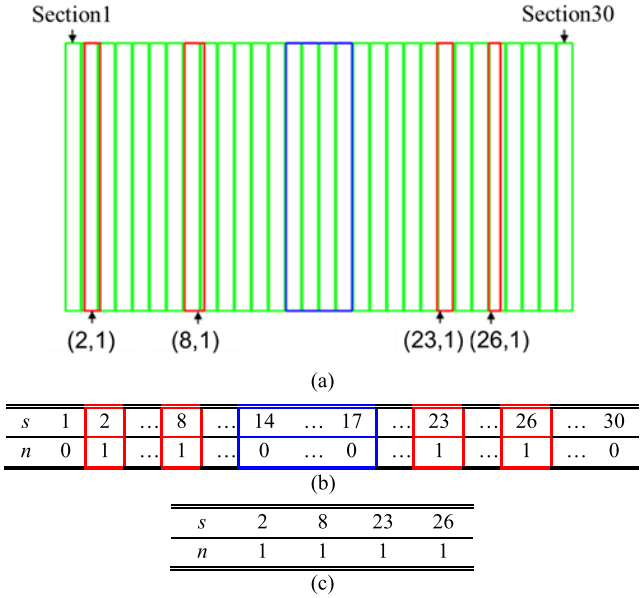

s	1	2	…	8	…	14	…	17	…	23	…	26	…	30
n	0	1	…	1	…	0	…	0	…	1	…	1	…	0

s	2	8	23	26
n	1	1	1	1

FIGURE 5. (a) One-dimensional section map consisting of 30 sections for genes (codes); (b) a chromosome composed of 30 genes; (c) chromosomes after the omission of sections with no gene codes.

To apply the GA for the optimal combination of SRAFs and the post-OPC target, this study used the sections in the section map [Fig. 5(a)] to memorize SRAF sites. The section size was determined by the designed minimum grid size, and the layout of the sections containing rectangles could be 1D or 2D. The designed grid size was 5 nm in this study. Each section in the section map was individually encoded to serve as genes constituting chromosomes, in which one chromosome accounts for one solution. Fig. 5 presents the encoding pattern for 30 sections in the 1D section map. The ROI on the photomask was divided into rectangular sections, and a section map was created from green rectangles. The features of each section in the section map were represented by two parameters, (s, n); s denotes section s of SRAF in the section map and n denotes the feature n deposited in section s. In this

example, the sections included in the pre-OPC target were marked by the blue rectangle, and the SRAFs were marked by red rectangles, of which four were placed in the 2nd, 8th, 23rd, and 26th sections. Under the assumption that these were the first deposited features, the four SRAFs, or featured genes on the section map, could be denoted as (2,1), (8,1), (23,1), and (26,1), respectively. Fig. 5(a) presents details for the chromosomes forming the integral section map. Fig. 5(b) displays the chromosomes, each formed by 30 genes (codes) corresponding to a 1D array $n \times 1$. To prevent the gene codes from being overly long when processing the 2D photomask patterns, which could cause the computations for the crossover and mutation operations in the GA to become highly complicated and time-consuming, the sections that did not contain SRAFs (i.e., $n = 0$) were omitted, as indicated in Fig. 5(c). The chromosomes were denoted in the simplified form of a 2D array, (s, n).

In a GA, a statistical population can yield an individual item by passing down its SRAFs through crossover and mutation processes. Under the assumption that a population contains two features, (s_1, n_1) and (s_2, n_2), a crossover process can be performed when the address of s_1 is equivalent to the address of s_2. Fig. 6 illustrates the crossover operations conducted for this study. Fig. 6(a) displays two parent populations, of which parent 2 is a simplified chromosome with no section codes of 0. Fig. 6(b) demonstrates the crossover process of the two chromosomes after the parent is extended to the same length as the binary-coded parent 1. The codes in the array of parent 1 (n_1) and parent 2 (n_2) are used for a random crossover, with the purple and red binary gene codes denoting the codes inherited from n_1 of parent 1 and n_2 of parent 2, respectively. Fig. 6(c) presents the resultant children 1 and children 2 chromosomes created through the crossover process. The mutation process can be illustrated by the example provided in Fig. 7, which displays the blue rectangle in the section map denotes the site of the target pattern, and the red rectangles represent SRAFs. The mutation process comprises four major operations, namely deletion, addition, exchange, and adjustment. Fig. 7(a) presents an initial population, or parent, with $s = 2$, 8, 23, and 26 representing potential sections for SRAF placement. Fig. 7(b) demonstrates the random deletion of features from the parent. For example, n changes from 1 to 0 when $s = 23$, indicating that it has been deleted. An addition operation represents the random addition of a feature that formerly appeared in other individuals but is not present in the current individual. For example, in Fig. 7 (c), n changes from 0 to 1 when $s = 29$, indicating that one SRAF has been added to the 29th section (chromosome). The exchange of features represents the random exchange of an innate feature with a different feature that was formerly present in the section. Fig. 7(d) provides an example in which the code $(s, n) = (8, 1)$ in the parent chromosome changes to $(s, n) = (8, 6)$. This indicates that at least 6 SRAFs have been deposited in this section. The adjustment operation involves randomly selecting an SRAF

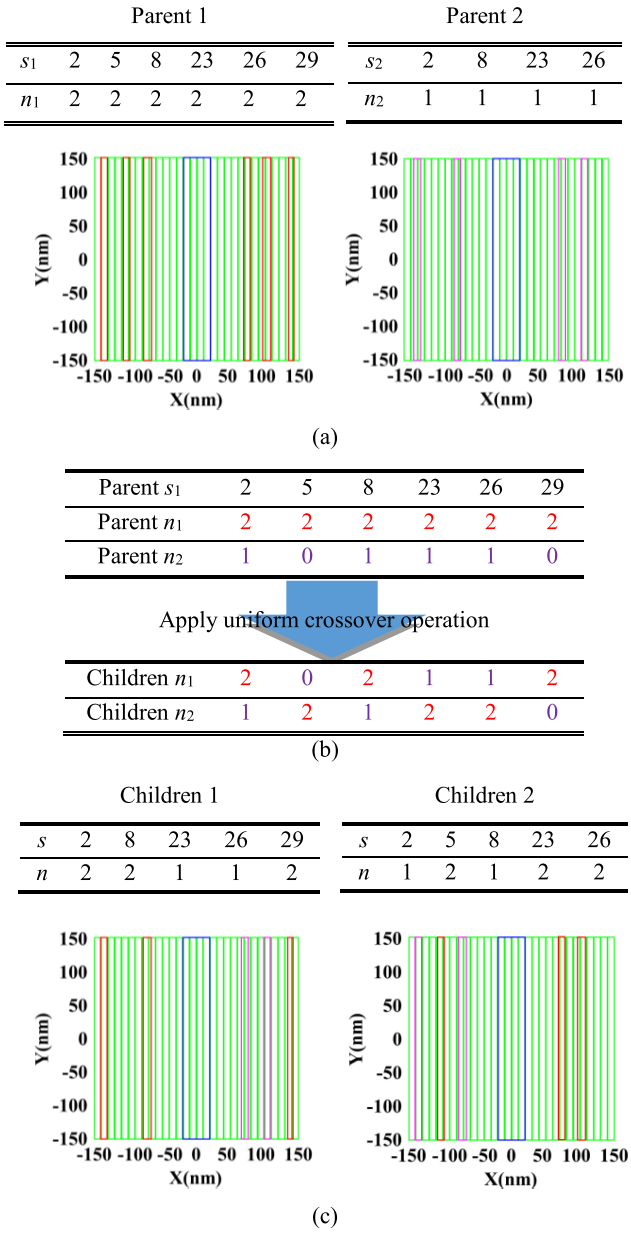

FIGURE 6. Crossover process of SRAFs: (a) gene codes of two parent SRAFs; (b) crossover process forming two children SRAFs; (c) two children SRAFs are decoded to create two photomasks.

to adjust its site and size, thus forming a new SRAF that differs from the original.

For example, in Fig. 7(d), n changes from 1 to 6 when $s = 8$, meaning that 5 SRAFs were originally deposited in this section but a 6th SRAF formed at section 8, that is $(s, n) = (8, 6)$, after adjusting the size and site of the SRAF at $(s, n) = (8, 1)$.

This study employed edge placement error (EPE) as the fitness function for GA optimization [46], [47], defining an arbitrary critical shape (CS) point on the target pattern as the displacement error from the aerial image contour (Fig. 8). Therefore, the fitness function can be expressed as (7),

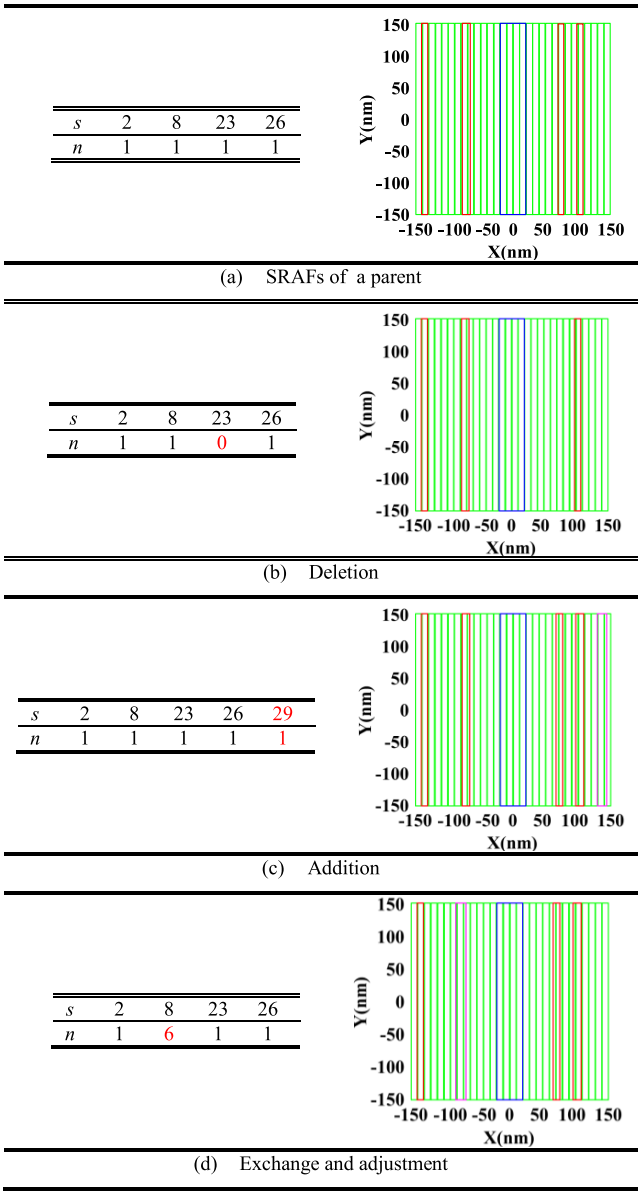

FIGURE 7. Four operations in the mutation process: (a) the SRAFs of a parent; (b) deletion; (c) addition; (d) exchange and adjustment.

introducing eight additional process conditions other than the nominal focus and nominal dose to define the upper and lower dose limits of the exposure energy and an acceptable DOF. Regarding the effect of the process variation band, w_{pw} denotes the EPE weight under different processing parameters, and w_j denotes the EPE weight of different CS points. The design of this fitness function ensures that the process window of the photomask images increases after the addition of new SRAFs.

$$F_{EPE} = \sum_{pw} w_{pw} \sum_{j} w_j \left\| EPE(x_j, pw) \right\|^p \tag{7}$$

Because an overly complicated photomask design increases the cost of the photomask, this study introduces a set of

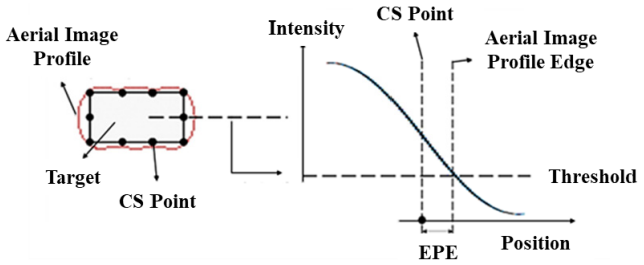

FIGURE 8. Calculation of the EPE of a CS point to the aerial image profile.

TABLE 1. Settings of the mask rules.

Feature	Rules	Figure of Rules
Bright Feature	$a_1 < W \le b_1$ & $H > c_1$, $W > b_1$ & $H > d_1$, $a_1 < b_1$, $c_1 < d_1$, W : feature width, H : feature height	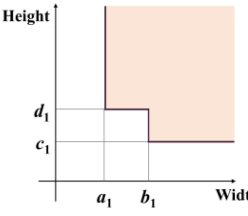
Dark Feature	$a_2 < W \le b_2$ & $H > c_2$, $W > b_2$ & $H > d_2$, $a_2 < b_2$, $c_2 < d_2$, W : feature width, H : feature height	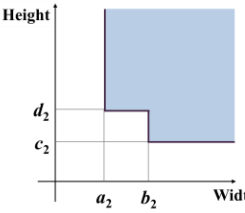
Distance Between Feature	$D \ge e$, D : distance between features	

mask rules to eliminate potential SRAFs that fail to meet its conditions. The mask rules applied in this study are listed in TABLE 1. These rules define the height–width relationship of rectangular features and the distance between them. When the photomask has a bright feature as the background, the feature width (W) must be between a_1 and b_1 and its height (H) must be greater than d_1. However, if $W > b_1$, H must be $>d_1$, $a_1 < b_1$, and $c_1 < d_1$. When the photomask has a dark feature as the background, $a_2 < W < b_2$ and $H > c_2$, but if $W > b_2$, H must be $>c_2$, $a_2 < b_2$, and $c_2 < d_2$. Additionally, the distance between features (D) must be greater than the minimum value e, irrespective of whether it has a dark or bright feature. After applying the mask rules, all of the SRAFs were simplified into rectangles and were in conformance with geometric dimensioning.

The GA-based SRAF design process is explained in TABLE 2. The first step involves calculating the interference and section maps, which are used to generate a potential SRAF set. Subsequently, each SRAF in the SRAF set is matched with a pre-OPC target, thus transforming the SRAF set into an initial population set, which is also the mask pattern set. Roulette wheel selection is then applied to select

TABLE 2. Pseudocode of GA-based SRAF design.

```
Algorithm: IMLGAO(M,S,P,GA,MaxIt)
Input: M  % Input layout
       S  % Source
       P  % a set of setting data
       GA % a set of GA parameters
       MaxIt % Max Iteration
IM ← Get_interference_map(M,S,P)
SM ← Get_section_map(M,P)
Pop ← Initial_population(IM,SM,P)
while It does not meet MaxIt
    for i ← 1 to GA.nc
        Parent ← RouletteWheelSelection(Pop.Cost)
        PCrossover.Gene ← Crossover(Parents.Gene, GA)
        PCrossover.Cost ← EvaluateFitness(Children, P)
    end for
    for i ← 1 to GA.nm
        Parent ← RouletteWheelSelection(Pop.Cost)
        PMutation.Gene ← Mutation(Parents.Gene,GA)
        PMutation.Cost ← EvaluateFitness(Children,P)
        SM ← update_sectionmap(SM,PMutation.Gene)
    end for
    Pop ← Pop ∪ PCrossover ∪ PMutation
    It ← It + 1
return Pop
```

n_c and n_m candidates (SRAF + pre-OPC target), respectively, from the initial population set, thus forming populations for the crossover and mutation processes. Simultaneously, OPC is conducted on pre-OPC targets to create post-OPC targets. The aerial image contour of each photomask image (SRAF + post-OPC target) is then calculated to determine its corresponding fitness, enabling the order of the candidates in the population set to be rearranged. The first 1000 individuals are selected to form a new population set for the optimization iterations, which are conducted until the aerial image meets all lithographic metric specifications. The lithographic metric specifications applied in this study were -10% <CD error $<10\%$ and exposure latitude (EL) $<5\%$ as the acceptable DOF [48].

IV. EXPERIMENTAL RESULTS

The convergence of the proposed GA was tested using a 1D L/S target pattern (CD = 45 nm, pitch = 300 nm), with an ArF immersion optical lithography system at a wavelength of 193 nm and an *NA* of 1.2. The light source was a dipolar source, with added transverse electric (TE) polarization, as displayed in Fig. 9(a). Fig. 9(b) displays the aerial image quality observed at a metrology site. Fig. 9(c) and Fig. 9(d) demonstrate the aerial image quality results obtained after the addition of GA-based SRAFs and after the PROLITH correction, respectively. In this test, the termination condition for the GA was set as reaching the maximum number of iterations, and the parameters are Max_Iteration = 200, population size $n_p = 30$, gene crossover ratio $p_c = 0.7$, gene mutation ratio $p_m = 0.3$, and single gene mutation ratio $m_u = 0.1$. Furthermore, the optical model in Section II was applied to generate an interference map and the SRAFs corresponding to the target pattern and thus produce an aerial image that

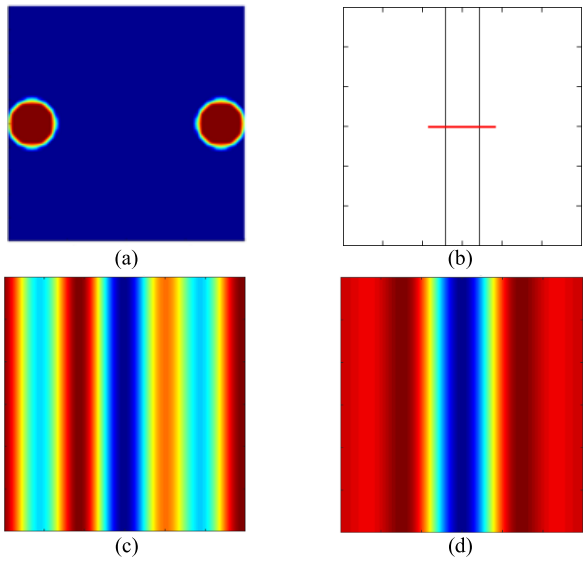

FIGURE 9. (a) Light source used in this test; (b) metrology site selected for assessing aerial image performance; (c) aerial image obtained by applying the GA; and (d) aerial image obtained by applying the PROLITH.

TABLE 3. Comparison of aerial image for 1D_L/S.

	With GA SRAF	W/O GA SRAF
CD (nm)	45.0	44.5
CD error (%)	0	-1.1
Contrast	0.86	0.92
NILS	2.72	3.08
DOF (nm)	147	88

combined the target pattern and SRAFs. This aerial image was then compared with the aerial image obtained by applying bias correction to the target pattern.

TABLE 3 summarizes the results of the predetermined metrology site. For the aerial image obtained with GA-generated SRAFs, CD was 45.0 nm, CD error was 0%, contrast was 0.86, and normalized image log-slope (NILS) was 2.72. Furthermore, under an EL of 5% and DOF of 147 nm, the aerial image obtained through the bias correction of the PROLITH without SRAF placement achieved a CD of 44.5 nm, CD error of -1.1%, contrast of 0.92, NILS of 3.08, and DOF of 88 nm when the EL was 5%. Fig. 10(a) compares the process windows of the two photomask images; the DOF of the photomask pattern created by combining GA-generated SRAFs and the target pattern was 67% greater than that without applying the SRAFs, proving that the generated SRAFs effectively supplemented the target pattern and had more favorable aerial image performance. Fig. 10(b) evaluates the degree of fitness of the GA-based iterations with the environment and convergence characteristics. EPE was used as the parameter for environmental fitness, and the results indicated that convergence was achieved by the 100th iteration.

This study further tested the two 2D patterns to determine if applying the GA would achieve better results in a dense area.

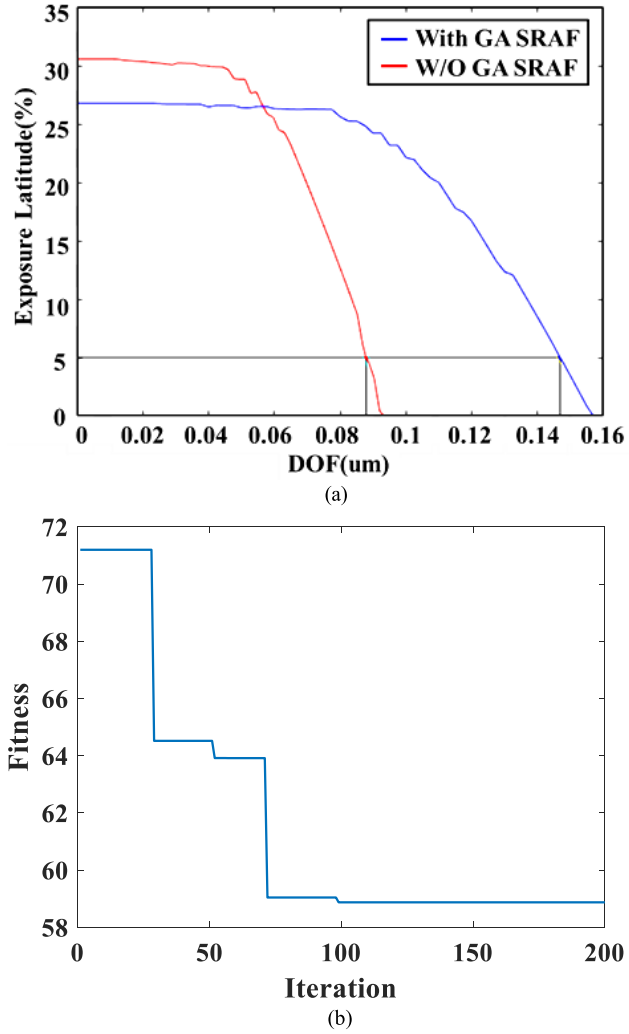

FIGURE 10. (a) EL compared with DOF results for the two aerial images; (b) number of iterations and corresponding environmental fitness parameters.

The line-space array was selected as the first pattern, and the contact hole (CH), which was relatively complicated and had a non-L/S pattern, was selected as the second. The GA was applied to add the SRAFs into the target pattern undergoing PROLITH-based OPC, which was compared with the photomask pattern produced by applying PROLITH-based OPC to the target pattern without the SRAF placement. The light source used in the test for the L/S array pattern was annular and had TE polarization, as shown in Fig. 11(a), with the wavelength for the ArF immersion optical lithography system set at 193 nm with an NA of 1.2. Fig. 11(b) demonstrates that the L/S array target pattern measured 1.7 × 4.2 um^2 on the phase-shift mask (PSM) which had a transmittance of 0.06 and phase shift of 180°. Aerial image performance was measured at 15 metrology sites, and the measurement results are indicated by the red lines in Fig. 11(b); the target line width in the L/S array should be 50 nm. The SRAF pattern design parameters for the L/S array were: maximum number of iterations of 300, population size n_p of 30, gene

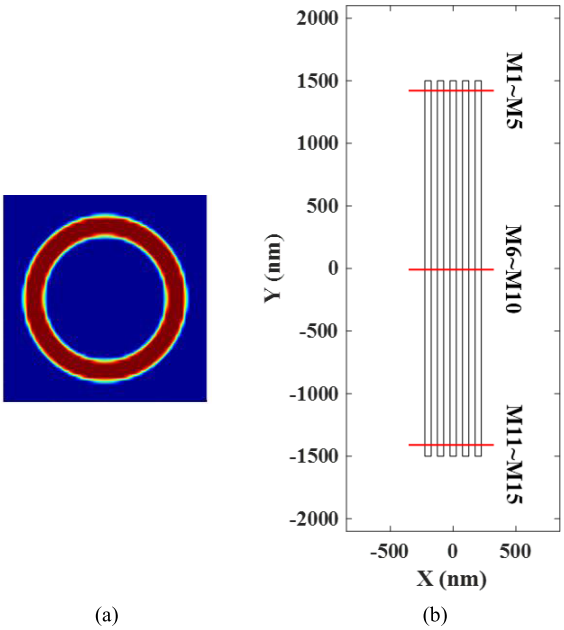

FIGURE 11. (a) Source used for exposing the L/S array pattern; (b) three metrology lines on the target pattern.

crossover ratio p_c of 0.6, gene mutation ratio p_m of 0.4, and single gene mutation ratio m_u of 0.2. The optimal solutions obtained with the GA-generated SRAFs, presented in Fig. 12(a), differ from the results of applying bias correction without addition of SRAFs, presented in (b). The aerial image contours of the two are illustrated in (c) and (d), respectively. As indicated in (c) and (d), the aerial image contour supplemented with the SRAFs exhibited significantly favorable performance because it was closer to the target pattern. By contrast, the aerial image contour obtained through the PROLITH-based OPC appears shrunken or dented on both ends and differs more noticeably from the target pattern.

TABLE 4. Comparison of the L/S_array aerial image results.

Bar	With GA SRAF			Without GA SRAF		
	CD error (%)	Contrast	NILS	CD error (%)	Contrast	NILS
M1	-2.0	0.504	1.330	-1.2	0.703	1.904
M2	-1.4	0.302	0.909	-1.4	0.292	0.826
M3	-1.8	0.272	0.841	-0.5	0.210	0.638
M4	-1.6	0.302	0.908	-1.6	0.293	0.819
M5	-2.0	0.504	1.332	-1.5	0.703	1.905
M6	0	0.500	1.337	0	0.724	2.005
M7	0	0.315	0.953	0.3	0.313	0.893
M8	0.1	0.290	0.899	0.1	0.227	0.696
M9	0.1	0.315	0.953	-0.1	0.312	0.888
M10	0	0.500	1.337	0	0.724	2.005
M11	-2.0	0.504	1.330	-1.0	0.704	1.900
M12	-1.6	0.302	0.909	-1.2	0.289	0.818
M13	-1.8	0.272	0.843	-2.2	0.204	0.626
M14	-1.8	0.302	0.907	-1.1	0.294	0.830
M15	-2.0	0.504	1.330	-1.9	0.704	1.904

TABLE 4 details the performance of the aerial image that used GA-generated SRAFs to supplement the target pattern.

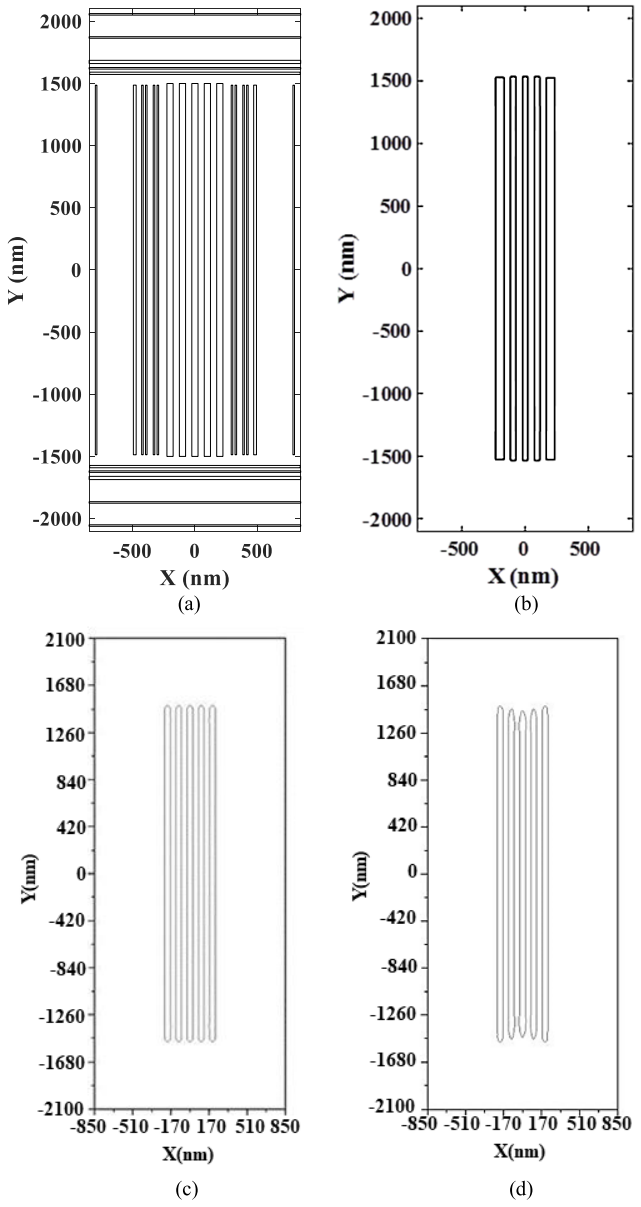

FIGURE 12. (a) Optimal photomask pattern obtained by the PROLITH-based OPC L/S pattern with SRAFs using the GA; (b) photomask pattern obtained by the PROLITH-based OPC L/S pattern only; (c) and (d) contours of aerial images with GA- generated SRAF and without GA-generated SRAF respectively.

The performance of this aerial image is also compared with that of the aerial image that has a target pattern and that only underwent PROLITH-based OPC. The compared items are the CD error, contrast, NILS, and DOF at an EL of 5%, measured at various sites. For the photomask pattern that was corrected by applying the GA, the CD error$_{avg}$ was 1.21% and the overall DOF was 188 nm. By contrast, for the photomask pattern that was corrected by applying PROLITH-based OPC, the CD error$_{avg}$ was 0.94% and overall DOF of the measurement lines was 75 nm. The common process

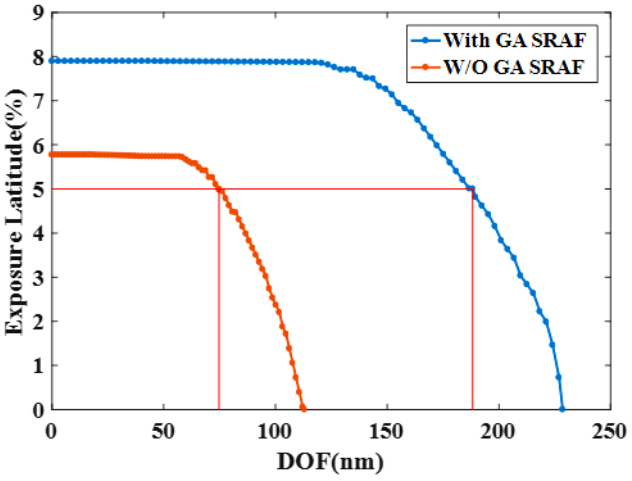

FIGURE 13. Comparison of the process windows of the L/S array that were enhanced by the GA and underwent OPC only. The blue line represents the results with GA SRAF and the orange line represents the results without GA SRAF.

window of each measurement site was calculated to compare the EL–DOF curves of the target patterns enhanced by the GA and the PROLITH-based OPC, the results of which are displayed in Fig. 13. For the tested L/S array pattern employed to achieve a larger process window, the contrast and NILS did not vary significantly by location. Therefore, the difference between the maximum and minimum contrast values is defined as Δcontrast for assessing the image quality; moreover, the GA-enhanced pattern achieved a Δcontrast of 0.232 and the PROLITH-based OPC pattern achieved a Δcontrast of 0.52. The same method of comparison was also applied to NILS; the GA-enhanced pattern achieved a ΔNILS of 0.496 and the PROLITH-based OPC pattern achieved a ΔNILS of 1.379. These results suggest that the GA-enhanced pattern outperformed the other pattern, enabling an overall increase in the DOF at an EL of 5% by 113 nm.

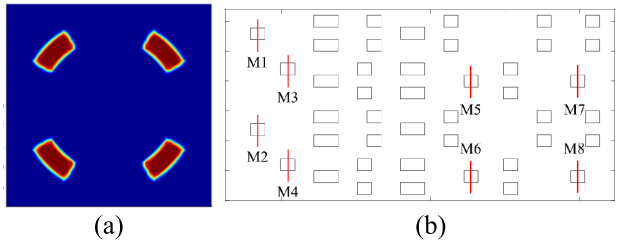

FIGURE 14. (a) Light source corresponding to the CH photomask; (b) target pattern for exposure simulation and the locations for measuring lines.

The second 2D pattern to be tested was the CH, which was tested using a quasar source, as depicted in Fig. 14(a). The ArF immersion optical lithography system was used with an NA of 0.93 to define the photomask pattern. Fig. 14(b) depicts the test clip, which measured 2.6 × 1.2 um^2.

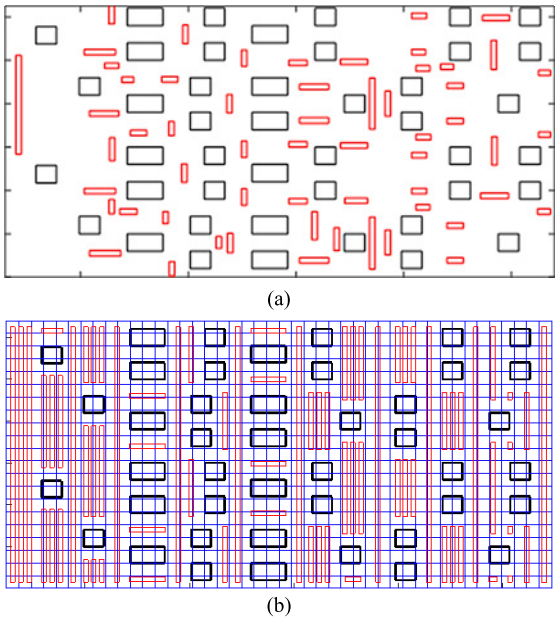

FIGURE 15. Potential SRAF sites on the CH clip identified using (a) the interference map; (b) the section map.

The PSM for the dark field had a transmittance of 0.06 and phase shift of 180°. The metrology sites were placed in the feature areas to observe the aerial images. A CD of 80 nm for the target pattern on the metrology sites is represented by the eight red lines in Fig. 14(b). The optical model discussed in Section II was used to calculate the CH interference map and thus identify the potential SRAF sites on the test clip; the results suggested that the potential sites were those indicated in Fig. 15. The black rectangles represent target patterns, and the red rectangles represent sites where an SRAF can be placed. The section map was then included to increase the number of potential SRAF sites, which should satisfy the MRC requirements. The sites are represented as red rectangles in Fig. 15(a). After the initial population of the CH patterns was generated, the GA was only able to generate 89 members of the initial population using the CH interference map because of weak inference signals. This necessitated the introduction of the section map. This helped to generate an initial population, which is represented by the set of blue rectangles in Fig. 15(b). Using the section map to randomly select potential SRAF sites enabled the addition of 1000 sites to the initial population. The parameters used for the CH in the GA were as follows: the population size n_p was 30, gene crossover ratio p_c was 0.6, gene mutation ratio p_m was 0.4, single gene mutation ratio m_u was 0.2, and maximum number of iterations was 200.

Fig. 16(a) depicts the optimal SRAF sites enhanced by the GA corresponding to the CH target pattern and Fig. 16(b) presents the aerial image identified as corresponding to the Fig. 16(a) mask pattern. For comparison, Fig. 16(c) displays

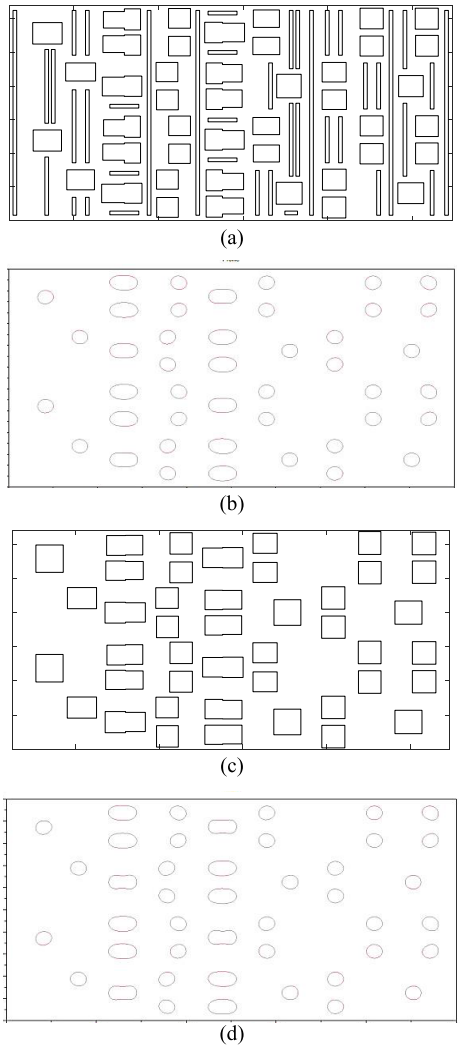

FIGURE 16. (a) Optimal CH pattern when applying the GA-generated SRAF; (b) aerial image contour corresponding to the (a) pattern; (c) optimal CH pattern when applying PROLITH-based OPC only; (d) aerial image contour corresponding to the (c) pattern.

the results of conducting OPC on the target pattern using PROLITH without adding SRAFs, and Fig. 16(d) presents the aerial image corresponding to the Fig. 16(b) mask pattern. A comparison of Fig. 16(b) and Fig. 16(d) suggests that the aerial image contour enhanced by the GA exhibited less asymmetry resulting in less discrepancy between the aerial image contour and target pattern contour. By contrast, the aerial image created from the photomask pattern that had only been enhanced through OPC exhibited more asymmetrical or dented features in the center and thus created a greater discrepancy between the aerial image contour and target pattern contour. These aerial image contours proved that the photomask pattern enhanced by the GA was superior to that only enhanced by PROLITH-based OPC. Further inspection of the process window of the pattern designed by applying the GA reveals the CD error, contrast, and NILS results for

TABLE 5. Summary of the CH pattern metrology site measurement results.

Bar	With GA SRAF			Without GA SRAF		
	CD error (%)	Contrast	NILS	CD error (%)	Contrast	NILS
M1	-1.9	0.481	1.025	-1.8	0.416	0.870
M2	-1.7	0.517	1.119	-2.1	0.416	0.861
M3	-0.6	0.583	1.236	-1.1	0.489	1.071
M4	-0.7	0.533	1.212	-0.3	0.488	1.068
M5	-1.0	0.467	1.041	-0.9	0.442	0.971
M6	-1.1	0.468	1.017	-1.1	0.443	0.967
M7	-0.4	0.511	1.094	-0.8	0.498	1.068
M8	-0.3	0.497	1.075	-1.2	0.497	1.057

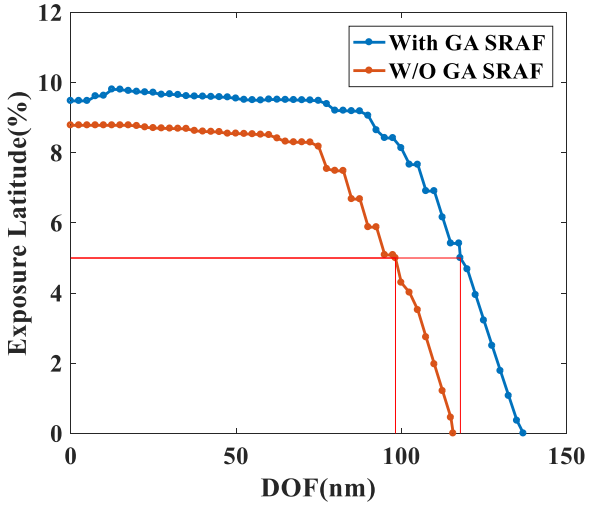

FIGURE 17. Comparison of the common process windows of the CH patterns designed by applying the GA and OPC. The blue line represents the SRAF results from applying the GA, and the orange line represents the SRAF results from applying OPC only.

various metrology sites in TABLE 5. The performance of the photomask pattern designed by applying the GA was as follows: the CD error$_{avg}$ was 0.96%, contrast$_{avg}$ was 0.507, and NILS$_{avg}$ was 1.102. The performance of the photomask pattern designed by applying OPC only was as follows: the CD error$_{avg}$ was 1.16%, contrast$_{avg}$ was 0.461, and NILS$_{avg}$ was 0.992. Fig. 17 compares the common process windows of metrology sites M1–M8: at an EL of 5%, the DOF was 118 nm for the photomask pattern designed by applying the GA and 98 nm for that designed by applying PROLITH-OPC only.

The performance of the GA-enhanced pattern was superior in terms of the common process window, as demonstrated in Fig. 17. The blue line represents the performance of the GA-enhanced pattern and the red line represents that of the PROLITH OPC-enhanced pattern. The results for both the L/S array and the CH patterns proved that the pattern designed by applying the GA had a greater DOF than that designed by applying OPC only. Therefore, the SRAFs generated with the GA can be considered to have improved the process window. In the GA calculations for the L/S array pattern, the EPE of the iterations continually decreased before

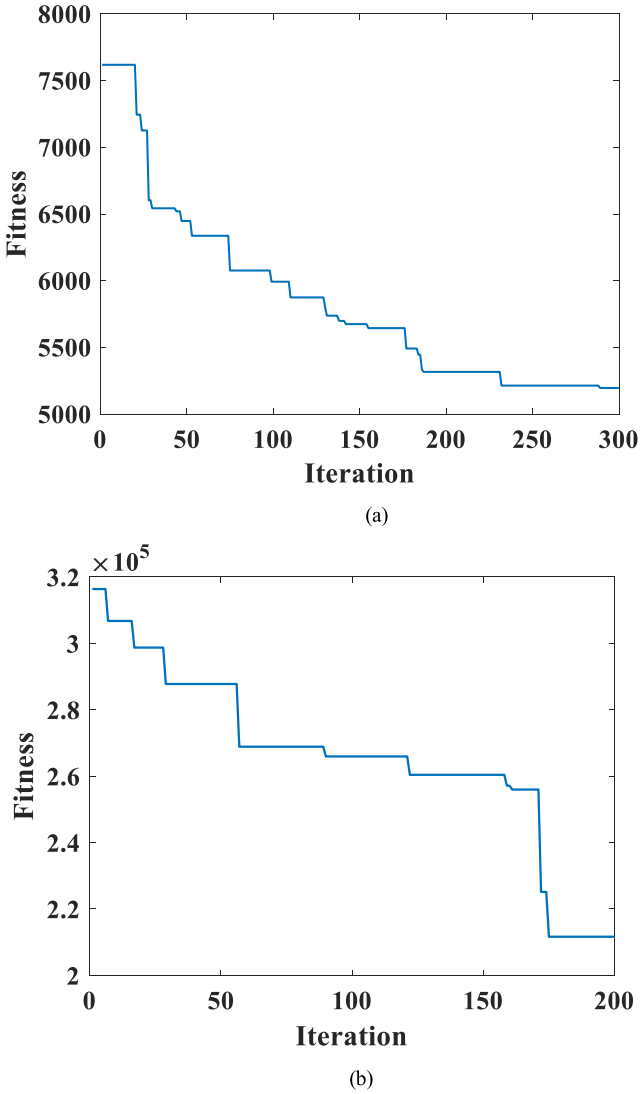

FIGURE 18. Convergence of the GA-based computation reflected in the relationship between EPE as fitness and the number of iterations. (a) Test results for the L/S array pattern; (b) test results for the CH pattern.

finally reaching convergence at the 280th iteration, as indicated in Fig. 18(a). However, in the case of the CH pattern, convergence was achieved at the 150th iteration, as indicated in Fig. 18(b).

V. CONCLUSION

This study successfully developed an GA-based method for performing geometric measurements and identifying SRAF placement. Test results from using 1D and 2D photomask patterns suggested that the process window had effectively increased. The strength of the proposed method is in its integration of the interference map and MRC, which enables potential SRAFs to serve as the initial population of the GA, thereby accelerating computation by reducing the range for SRAF searching. This study applied a design that used the GA for SRAFs that were rectangular in shape to reduce photomask cost. Additionally, because the fitness function

employed by the GA calculated the EPEs under nine processing steps, the designed pattern was a combination of SRAFs and the post-OPC target, which ensured that the process window would increase. This characteristic renders this method more practical for use by optical lithography engineers. It is recommended that in future studies, a machine learning model is introduced to determine the SRAF arrangement for specific target patterns. This could further improve computational efficiency.

ACKNOWLEDGMENT

The authors would like to thank KLA-Tencor for providing the Prolith simulator required to complete the numerical work.

REFERENCES

[1] K. K. Chang, P. J. Nair, D. Lee, S. Ghose, M. K. Qureshi, and O. Mutlu, "Low-cost inter-linked subarrays (LISA): Enabling fast inter-subarray data movement in DRAM," in *Proc. IEEE Int. Symp. High Perform. Comput. Archit. (HPCA)*, Mar. 2016, pp. 568–580.

[2] J. Jeddeloh and B. Keeth, "Hybrid memory cube new DRAM architecture increases density and performance," in *Proc. Symp. VLSI Technol. (VLSIT)*, Jun. 2012, pp. 87–88.

[3] S. Owa and H. Nagasaka, "Advantage and feasibility of immersion lithography," *J. Micro/Nanolithography, MEMS, MOEMS*, vol. 3, no. 1, pp. 97–104, Jan. 2004.

[4] D. P. Sanders, "Advances in patterning materials for 193 nm immersion lithography," *Chem. Rev.*, vol. 110, no. 1, pp. 321–360, Jan. 2010.

[5] W. Wang, L. Qin, Z. Yang, Y. Li, Z. Mao, and Y. Zhang, "Illumination optimization for lithography tools ope matching at 28 nm nodes," in *Proc. China Semiconductor Technol. Int. Conf. (CSTIC)*, Mar. 2017, pp. 1–4.

[6] F. M. Schellenberg, "Resolution enhancement technology: The past, the present, and extensions for the future," *Proc. SPIE*, vol. 5377, pp. 1–21, May 2004.

[7] L. Capodieci, "From optical proximity correction to lithography-driven physical design (1996-2006): 10 years of resolution enhancement technology and the roadmap enablers for the next decade," *Opt. Microlithography*, vol. 6154, no. 1, pp. 1–12, Mar. 2006.

[8] N. Zeggaoui, G. Landie, A. Villaret, V. Farys, E. Yesilada, A. Tritchkov, and J. Word, "Enabling the 14 nm node contact patterning using advanced RET solutions," in *Proc. 31st Eur. Mask Lithography Conf.*, vol. 9661, Jun. 2015, Art. no. 96610Q.

[9] Y. Ping, S. McGowan, Y. Gong, Y. M. Foong, J. Liu, J. Qiu, V. Shu, B. Yan, J. Ye, P. Li, H. Zhou, T. Pandey, J. Liang, C. Aquino, S. Baron, and S. Kapasi, "Process window enhancement using advanced RET techniques for 20 nm contact layer," *Proc. SPIE*, vol. 9052, Mar. 2014, Art. no. 90521N.

[10] N. B. Cobb and Y. Granik, "Model-based OPC using the MEEF matrix," in *Proc. 22nd Annu. BACUS Symp. Photomask Technol.*, vol. 4889, Dec. 2002, Art. no. 90520N.

[11] N. B. Cobb and Y. Granik, "OPC methods to improve image slope and process window," *Proc. SPIE*, vol. 5042, pp. 116–126, Jul. 2003.

[12] Q. Chen, Z. Mao, S. Yu, and W. Wu, "Sub-resolution-assist-feature placement study to dense patterns in advanced lithography process," in *Proc. China Semiconductor Technol. Int. Conf. (CSTIC)*, Mar. 2016, pp. 1–3.

[13] S. Ishida, S. Hashimoto, T. Yasuzato, and K. Kasama, "DOF enhancement effect of attenuated assist feature," *Proc. SPIE*, vol. 2793, pp. 34–43, Jul. 1996.

[14] L. S. Melvin, J. P. Mayhew, B. D. Painter, and L. D. Barnes, "Assist feature placement analysis using focus sensitivity models," in *Proc. 22nd Eur. Mask Lithograph Conf. (EMLC)*, Jan. 2006, pp. 1–7.

[15] B. Yenikaya, O. Alexandrov, S. Chen, A. Liu, A. Mokhberi, and A. Sezginer, "Model-based assist features," *Proc. SPIE*, vol. 7488, pp. 1–6, Sep. 2009.

[16] T. Li and Y. Li, "Lithographic source and mask optimization with low aberration sensitivity," *IEEE Trans. Nanotechnol.*, vol. 16, no. 6, pp. 1099–1105, Nov. 2017.

[17] M. Hakko, K. Yamazoe, M. Kawashima, Y. Sekine, M. Ohta, and T. Honda, "Extension of the 2D-TCC technique to optimize mask pattern layouts," *Proc. SPIE*, vol. 7028, May 2008, Art. no. 70280Z.

[18] K. Yamazoe, Y. Sekine, and T. Honda, "Aerial image back propagation with two-dimensional transmission cross coefficient," *J. Micro/Nanolithography, MEMS, MOEMS*, vol. 8, no. 3, Jul. 2009, Art. no. 031406.

[19] Y. Peng, J. Zhang, Y. Wang, and Z. Yu, "Gradient-based source and mask optimization in optical lithography," *IEEE Trans. Image Process.*, vol. 20, no. 10, pp. 2856–2864, Oct. 2011.

[20] X. Ma, Z. Wang, X. Chen, Y. Li, and G. R. Arce, "Gradient-based source mask optimization for extreme ultraviolet lithography," *IEEE Trans. Comput. Imag.*, vol. 5, no. 1, pp. 120–135, Mar. 2019.

[21] Y. Xu, B. Zhang, C. Wang, W. Wilkinson, and J. Bolton, "The performance improvement of SRAF placement rules using GA optimization," *Proc. SPIE*, vol. 9985, Oct. 2016, Art. no. 99851C.

[22] B. G. Kim, S. S. Suh, B.-S. Kim, S.-G. Woo, H.-K. Cho, V. Tolani, G. Dai, D. Irby, K. Wang, G. Xiao, D. Kim, K.-H. Baik, and B. Gleason, "Trade-off between inverse lithography mask complexity and lithographic performance," *Proc. SPIE*, vol. 7379, Jun. 2009, Art. no. 73791M.

[23] Y.-H. Su, Y.-C. Huang, L.-C. Tsai, Y.-W. Chang, and S. Banerjee, "Fast lithographic mask optimization considering process variation," *IEEE Trans. Comput.-Aided Des. Integr. Circuits Syst.*, vol. 35, no. 8, pp. 1345–1357, Aug. 2016.

[24] A. Awad, A. Takahashi, S. Tanaka, and C. Kodama, "A fast process-variation-aware mask optimization algorithm with a novel intensity modeling," *IEEE Trans. Very Large Scale Integr. (VLSI) Syst.*, vol. 25, no. 3, pp. 998–1011, Mar. 2017.

[25] C. Mack, *Fundamental Principles of Optical Lithography: The Science of Microfabrication*. Hoboken, NJ, USA: Wiley, 2008.

[26] H. H. Hopkins, "On the diffraction theory of optical images," *Proc. Roy. Soc. A*, vol. 217, no. 1130, pp. 408–432, May 1953.

[27] M. Mansuripur, *Classical Optics and Its Applications*. Cambridge, U.K.: Cambridge Univ. Press, 2002.

[28] M. Born and E. Wolf, *Principles of Optics: Electromagnetic Theory of Propagation, Interference and Diffraction of Light*. Amsterdam, The Netherlands: Elsevier, 2013.

[29] K. Yamazoe, Y. Sekine, M. Kawashima, M. Hakko, T. Ono, and T. Honda, "Resolution enhancement by aerial image approximation with 2D-TCC," *Proc. SPIE*, vol. 6730, Oct. 2007, Art. no. 67302H.

[30] K. Tsujita, T. Arai, H. Ishii, Y. Gyoda, K. Takahashi, V. Axelrad, and M. C. Smayling, "Supreme lithographic performance by simple mask layout based on lithography and layout co-optimization," *Proc. SPIE*, vol. 7973, Mar. 2011, Art. no. 79730D.

[31] M. Kawashima, K. Yamazoe, Y. Sekine, M. Hakko, M. Ohta, and T. Honda, "Mask optimization for arbitrary patterns with 2D-TCC resolution enhancement technique," *Proc. SPIE*, vol. 6924, Mar. 2008, Art. no. 69240F.

[32] R. J. Socha, D. J. Van Den Broeke, S. D. Hsu, J. F. Chen, T. L. Laidig, N. Corcoran, U. Hollerbach, K. E. Wampler, X. Shi, and W. Conley, "Contact hole reticle optimization by using interference mapping lithography (IML)," *Proc. SPIE*, vol. 5377, pp. 222–241, May 2004.

[33] L. D. Barnes, B. D. Painter, and L. S. Melvin, "Model-based placement and optimization of subresolution assist features," *Proc. SPIE*, vol. 6154, Mar. 2006, Art. no. 61542C.

[34] S. Das and P. N. Suganthan, "Differential evolution: A survey of the state-of-the-art," *IEEE Trans. Evol. Comput.*, vol. 15, no. 1, pp. 4–31, Feb. 2011.

[35] J. Kennedy, "Particle swarm optimization," *Encyclopedia Mach. Learn.*, pp. 760–766, 2010.

[36] J. Jägersküpper, "How the $(1 + 1)$ ES using isotropic mutations minimizes positive definite quadratic forms," *Theoretical Comput. Sci.*, vol. 361, no. 1, pp. 38–56, Aug. 2006.

[37] J. Fulcher, "Computational intelligence: An introduction," in *Computational Intelligence: A Compendium*, vol. 115. Berlin, Germany: Springer, 2008, pp. 3–78.

[38] T. Back, D. B. Fogel, and Z. Michalewicz, *Evolutionary Computation 1: Basic Algorithms and Operators*. Boca Raton, FL, USA: CRC Press, 2018.

[39] S. S. J. Owais, P. Krömer, and V. Snášel, "Query optimization by genetic algorithm," *J. Inf. Technol. Eng.*, vol. 3, no. 1, pp. 44–51, Jan. 2012.

[40] M. B. Bashir and A. Nadeem, "Improved genetic algorithm to reduce mutation testing cost," *IEEE Access*, vol. 5, pp. 3657–3674, 2017.

[41] E. J. Anderson and M. C. Ferris, "Genetic algorithms for combinatorial optimization: The assemble line balancing problem," *ORSA J. Comput.*, vol. 6, no. 2, pp. 161–173, May 1994.

[42] M. Srinivas and L. M. Patnaik, "Genetic algorithms: A survey," *Computer*, vol. 27, pp. 17–26, Jun. 1994.
[43] P. Rocca, G. Oliveri, and A. Massa, "Differential evolution as applied to electromagnetics," *IEEE Antennas Propag. Mag.*, vol. 53, no. 1, pp. 38–49, Feb. 2011.
[44] W. B. Langdon and R. Poli, *Foundations of Genetic Programming*. Berlin, Germany: Springer, 2013.
[45] B. Santosa and M. K. Ningrum, "Cat swarm optimization for clustering," in *Proc. Int. Conf. Soft Comput. Pattern Recognit.*, Dec. 2009, pp. 54–59.
[46] F. Lie, C.-Y. Huang, C.-S. Wu, K.-T. Chen, and H.-F. Kuo, "Demonstration of ACO-based freeform source for ArF laser immersion lithography system," *IEEE Access*, vol. 5, pp. 6421–6428, 2017.
[47] H.-F. Kuo, "Ant colony optimization-based freeform sources for enhancing nanolithographic imaging performance," *IEEE Trans. Nanotechnol.*, vol. 15, no. 4, pp. 599–606, Jul. 2016.
[48] C. A. Mack, *Inside PROLITH: A Comprehensive Guide to Optical Lithography Simulation*. Austin, TX, USA: FINLE Technologies, 1997.

WEI-MING KAN received the M.S. degree with the Graduate Institute of Automation and Control, National Taiwan University of Science and Technology, Taipei, in 2019.

YU-RU HUANG received the M.S. degree with the Graduate Institute of Automation and Control, National Taiwan University of Science and Technology, Taipei, in 2018.

CHAO-YI HUANG received the B.A. degree in physics from National Cheng Kung University, Tainan, Taiwan, and the M.S. degree from the Graduate Institute of Physics, National Chung Cheng University, Chia-Yi, Taiwan, in 1996. He is currently the Manager of the module process technology development of memory products with Winbond Electronics Corporation, Taiwan. His professional research interests include next-generation microlithography technology, optoelectronic metrology, and nano-optic applications.

CHUN-SHENG WU received the M.S. degree in chemical engineering from the National Taiwan University of Science and Technology, Taipei, Taiwan, in 1994. From 1995 to 1996, he served as a Platoon Leader (second lieutenant) in the army. From 1997 to 1999, he was a Process Engineer with Taisil Electronic Materials Corporation. Since 2000, he has been the Manager of microlithography development of memory products with Winbond Electronics Corporation, Taiwan. His research interests include lithography resolution enhancement technologies as well as flow integration and optimization from design to mask making.

KAO-TUN CHEN received the B.A. degree from the Department of Civil Engineering, National Taiwan University, Taipei, Taiwan, and the M.S. degree from the Graduate Institute of Structural Engineering, National Taiwan University. From 2004 to 2012, he was an OPC Development Engineer with the Nanolithography Department, Powerchip Technology Corporation. Since 2012, he has been the Manager of the microlithography development of memory products with Winbond Electronics Corporation, Taiwan. His professional research interests include next-generation microlithography technology and nano-optic applications.

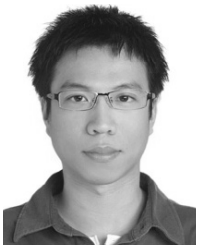

YU-SHIN LIN received the M.S. degree in optomechatronics engineering from National Central University, Taiwan, in 2007. Since 2008, he has been with Shuz Tung Machinery Industrial Company Ltd., Taichung, Taiwan. His research interests include the development of next generation machine techniques and control systems.

HUNG-FEI KUO received the Ph.D. degree in electrical and computer engineering from Georgia Institute of Technology, Atlanta, GA, USA, in 2004. From 2005 to 2006, he served as an Optical Department Manager with GCC, Taiwan. From 2007 to 2009, he was an Application Development Engineer with the ASML Center of Excellence, Taiwan. Since 2010, he has been a Faculty Member with the Graduate Institute of Automation and Control, National Taiwan University of Science and Technology, Taipei. His research interests include the development of next-generation lithography techniques and optical system integrations.